GFZ
Helmholtz-Zentrum
POTSDAM

Originally published as:

Huang, F., Juhlin, C., Han, L., Kempka, T., Lueth, S., Zhang, F. (2016): Quantitative evaluation of thin-layer thickness and CO2 mass utilizing seismic complex decomposition at the Ketzin CO2 storage site, Germany. - *Geophysical Journal International*, *207*, 1, pp. 160—173.

DOI: http://doi.org/10.1093/gji/ggw274

Geophysical Journal International

Geophys. J. Int. (2016) **207,** 160–173
Advance Access publication 2016 July 27
GJI Marine geosciences and applied geophysics

doi: 10.1093/gji/ggw274

Quantitative evaluation of thin-layer thickness and CO_2 mass utilizing seismic complex decomposition at the Ketzin CO_2 storage site, Germany

Fei Huang,[1] Christopher Juhlin,[1] Li Han,[2] Thomas Kempka,[3] Stefan Lüth[3] and Fengjiao Zhang[1,4]

[1]*Department of Earth Sciences, Uppsala University, Villavägen* 16, *Uppsala* 75236, *Sweden. E-mail: fei.huang@geo.uu.se*
[2]*Overseas Evaluation Center, CNOOC Research Institute, Taiyanggong South Street* 6, *Beijing* 100028, *China*
[3]*Helmholtz Centre Potsdam, GFZ German Research Centre for Geosciences, Telegrafenberg, D-*14473 *Potsdam, Germany*
[4]*College of Geoexploration Science and Technology, Jilin University, Xi Min Zhu Street No.* 938, *Changchun* 130026, *China*

Accepted 2016 July 20. Received 2016 July 12; in original form 2016 April 10

SUMMARY

Determining thin layer thickness is very important for reservoir characterization and CO_2 quantification. Given its high time–frequency resolution and robustness, the complex spectral decomposition method was applied on time-lapse 3-D seismic data from the Ketzin pilot site for CO_2 storage to evaluate the frequency-dependent characteristics of thin layers at the injection level. Higher temporal resolution and more stratigraphic details are seen in the all-frequency and monochromatic reflectivity amplitude sections obtained by complex spectral decomposition compared to the stacked sections. The mapped geologic discontinuities within the reservoir are consistent with the preferred orientation of CO_2 propagation. Tuning frequency mapping shows the thicknesses of the reservoir sandstone and gaseous CO_2 is consistent with the measured thickness of the sandstone unit from well logging. An attempt to discriminate between pressure effects and CO_2 saturation using the extracted tuning frequency indicates that CO_2 saturation is the main contributor to the amplitude anomaly at the Ketzin site. On the basis of determined thickness of gaseous CO_2 in the reservoir, quantitative analysis of the amount of CO_2 was performed and shows a discrepancy between the injected and calculated CO_2 mass. This may be explained by several uncertainties, like structural reservoir heterogeneity, a limited understanding of the complex subsurface conditions, error of determined tuning frequency, the presence of ambient noise and ongoing CO_2 dissolution.

Key words: Image processing; Fourier analysis; Inverse theory; Computational seismology.

1 INTRODUCTION

Carbon capture and storage is a comparatively cost-effective technology for preventing substantial amounts of CO_2 from entering into the atmosphere in the next several decades. The Ketzin site, serving as the first European onshore pilot-scale CO_2 storage site, is situated on the southern flank of the Ketzin anticline, approximately 25 km west of Berlin, Germany (Fig. 1). In 2007, three wells (one injection well, Ktzi 201 and two observation wells, Ktzi 200 and Ktzi 202) were drilled to a depth of 750 m to 800 m with a distance of 50–110 m from each other. In 2012, another observation well, Ktzi 203, was drilled to a depth of 700 m with a distance of 25 m from Ktzi 201 (Liebscher & Münch 2015). Injection of CO_2 started in June 2008 and ceased in August 2013 (Martens *et al.* 2014). A total of about 67 kt of CO_2 was injected into the 633–652 m deep sandstone channels of a saline aquifer in the 75–80-m-thick Stuttgart Formation of Triassic age. Muddy, flood-plain-facies (poor reservoir quality) alternates with sandy channel-facies (good reservoir quality) in the heterogeneous Stuttgart Formation. The immediate caprock of the reservoir formation is formed by the 210-m-thick Weser and Arnstadt formations consisting of mudstones and anhydritic mudstones (Norden *et al.* 2010). A 10–20-m-thick anhydrite layer with low porosity and permeability is present at the top of the Weser formation.

Quantitative assessment of the injected CO_2 is very important for CO_2 geological storage projects to demonstrate that the injected CO_2 injected remains in the reservoir (Arts *et al.* 2002; Chadwick *et al.* 2005; Lüth *et al.* 2015). In addition, if CO_2 leaks into the overlying formations, quantitative estimation of CO_2 leakage is required for designing the most effective remediation and mitigation strategies (Ivanova *et al.* 2012). However, several limiting factors, like thin layers and limited vertical resolution exist, making quantitative seismic analysis difficult at CO_2 storage sites. This is due to several factors. First, CO_2 storage within saline aquifers

© The Authors 2016. Published by Oxford University Press on behalf of The Royal Astronomical Society.

Downloaded from http://gji.oxfordjournals.org/ at Bibliothek des Wissenschaftsparks Albert Einstein on September 19, 2016

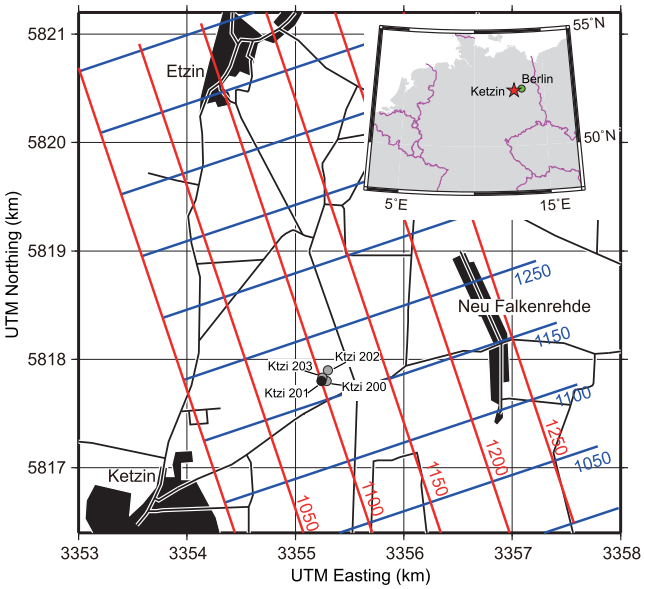

Figure 1. 3-D seismic survey area with inlines (blue lines) and crosslines (red lines). The locations of the injection well (Ktzi 201) and three observation wells (Ktzi 200, Ktzi 202 and Ktzi 203) are marked by the black and grey dots, respectively. Inset shows the location of the Ketzin pilot site for CO_2 storage in Germany.

often exploits thin high-permeability layers (such as palaeochannels or sandstone channels; Johansson *et al*. 2012). Second, buoyancy-driven CO_2 migrates laterally along the top of the reservoir, forming a new thin layer. Third, active band-limited seismic methods utilizing impedance change and reflection time pushdown can detect CO_2 accumulations, but have difficulties in estimating the thickness of thin layers. As an onshore CO_2 storage experiment in a semi-urban site, ambient noise generated by human activities at the Ketzin pilot site is inevitable. In addition, the presence of the thin high-velocity (around 5500 m s^{-1}) anhydrite layer masks the layers below, in particular the reservoir layer with weak reflection energy, challenging the use of conventional seismic studies (reflection, refraction and passive seismic).

Since the CO_2 plume has analogous characteristics to a thin bed, a number of approaches have been developed in order to estimate the thickness of the injected CO_2 plume from seismic surveys (Chadwick *et al*. 2009; Sturton *et al*. 2010; Arts & Eyvazi 2011). Arts *et al*. (2004a), Chadwick *et al*. (2004) and Ghaderi & Landrø (2009) utilized seismic amplitude and time shift to estimate the layer thickness of CO_2 at the Sleipner project site, but if phase and amplitude are not well preserved during the data processing errors may be large. As an alternative, spectral decomposition is an effective time–frequency analysis tool for decomposing seismic signals into discrete-frequency components which are phase-independent. The thickness can be determined based on the relationship between the tuning frequency and temporal thickness using spectral decomposition. Several spectral decomposition methods, such as the continuous wavelet transform (CWT) and the Wigner–Ville distribution, have been applied to CO_2 storage sites to qualitatively and quantitatively assess the injected CO_2 (Chadwick *et al*. 2010; Ravazzoli & Gómez 2014). White *et al*. (2013) used the smoothed pseudo Wigner–Ville distribution (SPWVD) to analyse the topmost supercritical CO_2 layer at the Sleipner gas field. A spectral inversion method was also performed, but with limited success. Williams & Chadwick (2012) tested the potential of using SPWVD to estimate the thickness and velocities of thin layers of CO_2 in the Sleipner injection plume. The same spectral decomposition method was also applied at the Snøhvit gas field to distinguish between seismic anomalies caused by CO_2 saturation and pressure (White *et al*. 2015).

In this study, we aim to utilize spectral decomposition to quantitatively analyse the thickness of a thin reservoir and gaseous CO_2 distribution at the Ketzin pilot site. Previously, Kazemeini *et al*. (2009) applied the CWT in order to qualitatively detect sandstone channels in the Stuttgart Formation and remnants of natural gas stored in Jurassic formations. Huang *et al*. (2016) extracted wavelet phase changes using complex spectral decomposition (Bonar & Sacchi 2010) to map CO_2 migration and possible sandstone channels. Compared with conventional spectral decomposition techniques, the complex spectral decomposition strategy has higher time–frequency resolution and appears to be less sensitive to noise (Han *et al*. 2015; Liu *et al*. 2015; Huang *et al*. 2016). Considering the specific limitations at the Ketzin pilot site, complex spectral decomposition is a good candidate for quantitatively analysing the amount of gaseous CO_2 within the reservoir.

We first uses a synthetic example to verify the effectiveness and robustness of the complex spectral decomposition method. Then monochromatic reflectivity data are decomposed from the 3-D time-lapse seismic data from the Ketzin pilot site using complex spectral decomposition to show how the reservoir response varies at distinct frequencies. After wavelet spectrum balancing, a group of frequency slices of the reservoir tuning cube is extracted to investigate thin-bed interference. By using the relationship between the temporal thickness and tuning frequency, the thickness of the reservoir sandstone and gaseous CO_2 are determined, and consequently the gaseous CO_2 mass within the reservoir is calculated. Finally, uncertainties related to seismic quantitative interpretation are discussed.

2 APPLICATION OF COMPLEX SPECTRAL DECOMPOSITION TO DATA FROM THE KETZIN PILOT SITE FOR CO_2 STORAGE

Complex spectral decomposition (Bonar & Sacchi 2010; Han *et al*. 2015) is a spectral decomposition method using inversion strategies to decompose the seismic signal into the corresponding complex time–frequency spectrum which includes the phase and frequency information (Appendix). Unlike spectral decomposition methods based on Fourier and wavelet transforms, the complex spectral decomposition method is less restricted by the Heisenberg–Gabor uncertainty principle (Gabor 1946; see Fig. A1). A complex Ricker wavelet library is used in this study because (1) the wavelet extracted from the processed 3-D seismic data at the Ketzin site using a statistical method is very close to a Ricker wavelet; (2) the seismic trace can be well reconstructed by convolving the reflectivity series obtained by complex spectral decomposition with the chosen wavelet library. This section shows the application of the complex spectral decomposition method to the time-lapse 3-D data sets in order to quantitatively assess the amount of injected CO_2 at the Ketzin pilot site.

In autumn 2005, a 3-D seismic survey, serving as a baseline, was acquired (Juhlin *et al*. 2007), followed by two 3-D repeat seismic surveys (Ivanova *et al*. 2012; Ivandic *et al*. 2015) in 2009 and 2012 after injection of around 23.5 and 61 kt of CO_2, respectively. Before performing spectral decomposition on the time-lapse 3-D seismic data, the two repeat volumes acquired in 2009 and 2012 were cross-calibrated by employing the baseline as a reference

Downloaded from http://gji.oxfordjournals.org/ at Bibliothek des Wissenschaftsparks Albert Einstein on September 19, 2016

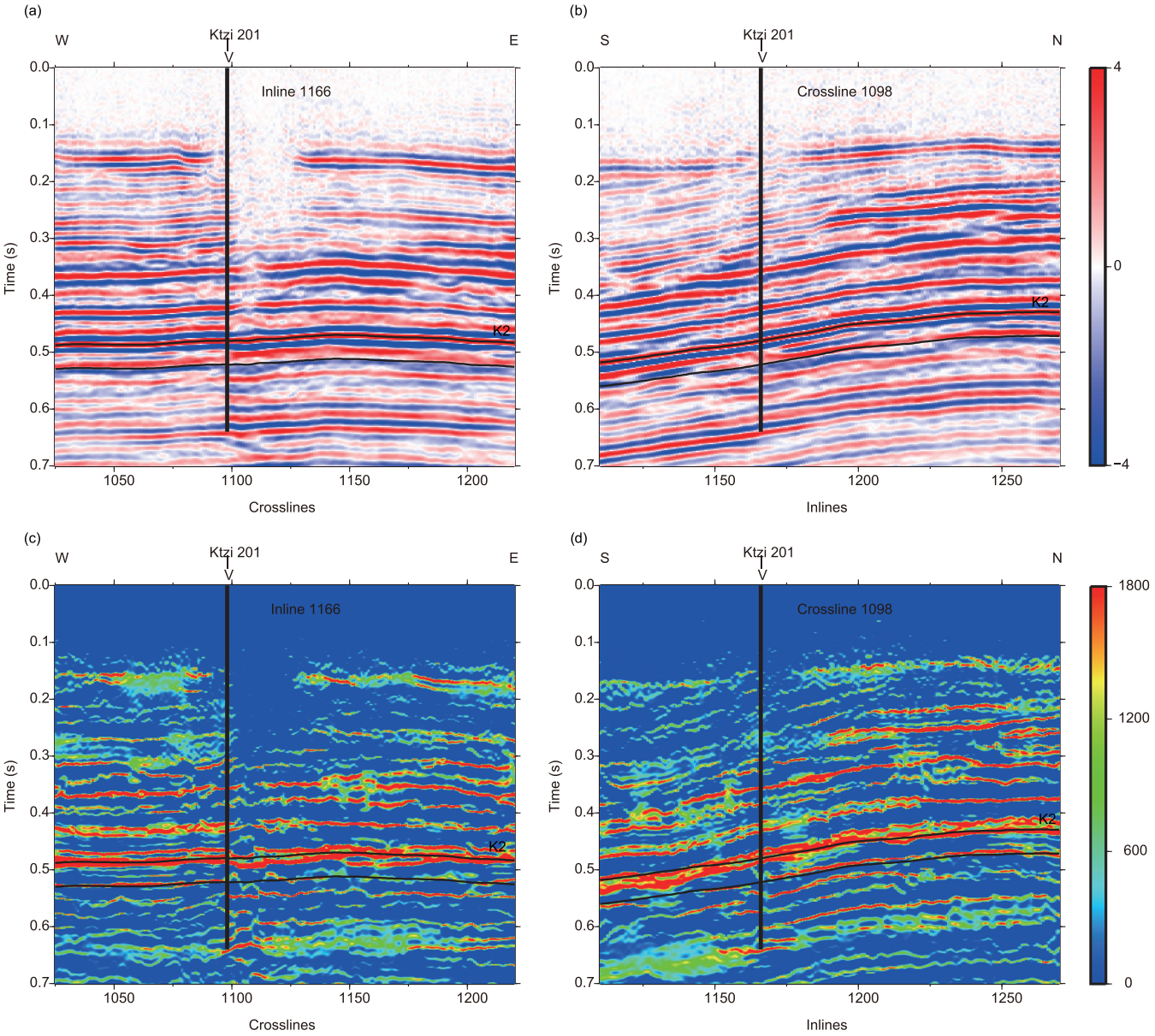

Figure 2. Seismic sections along (a) inline 1166 and (b) crossline 1098, and the corresponding reflectivity amplitude sections at all frequency bands along (c) inline 1166 and (d) crossline 1098. The location of the injection well is marked by the black vertical line. The black horizontal lines represent the approximate locations of the K2 reflector and reservoir, respectively.

volume in order to minimize the non-injection related anomalies (Ivanova *et al*. 2012; Ivandic *et al*. 2015). Fig. 2 shows the baseline seismic amplitude sections adjacent to the injection well and the corresponding reflectivity amplitude sections at all frequency bands. The pronounced reflection marked as K2 results from the thin anhydrite layer above the reservoir. It is clear that an improvement in temporal resolution is achieved by applying complex spectral decomposition when compared with the conventional seismic data. More stratigraphic details are visible in the reflectivity amplitude sections. Discontinuities in the reservoir horizon, especially to the east and south of the site, are consistent with the presence of a highly heterogeneous reservoir and explain the observed predominant WNW trend in the CO_2 plume migration (Ivandic *et al*. 2015).

In order to use frequency as a tuning button to obtain a first visual estimate of layer thicknesses, a group of monochromatic reflectivity amplitude sections have been extracted from the baseline and two repeat seismic data sets (Fig. 3). Most of the reflectivity amplitudes related to the reservoir are present between the dominant frequencies of 30 and 40 Hz, while the reflectivity amplitude of the K2 reflector is more obvious at 40 Hz. For frequencies below 30 Hz or above 50 Hz, the amplitude becomes very low and may only represent ambient noise. Amplitude anomalies due to the injected CO_2 in the repeat surveys are more noticeable at a dominant frequency of 40 Hz. Fig. 4 shows the 40 Hz horizon maps of the reflectivity amplitude and the corresponding wavelet phase at the reservoir level. Phases corresponding to very low reflectivity amplitudes (less than 25 per cent of the maximum amplitude) which are widespread over the map are assumed to be due to the remaining non-repeatable noise and were removed (Ivandic *et al*. 2015; Huang *et al*. 2016). This study focuses on the application of the frequency attributes, however, by combining both reflectivity amplitude and

Downloaded from http://gji.oxfordjournals.org/ at Bibliothek des Wissenschaftsparks Albert Einstein on September 19, 2016

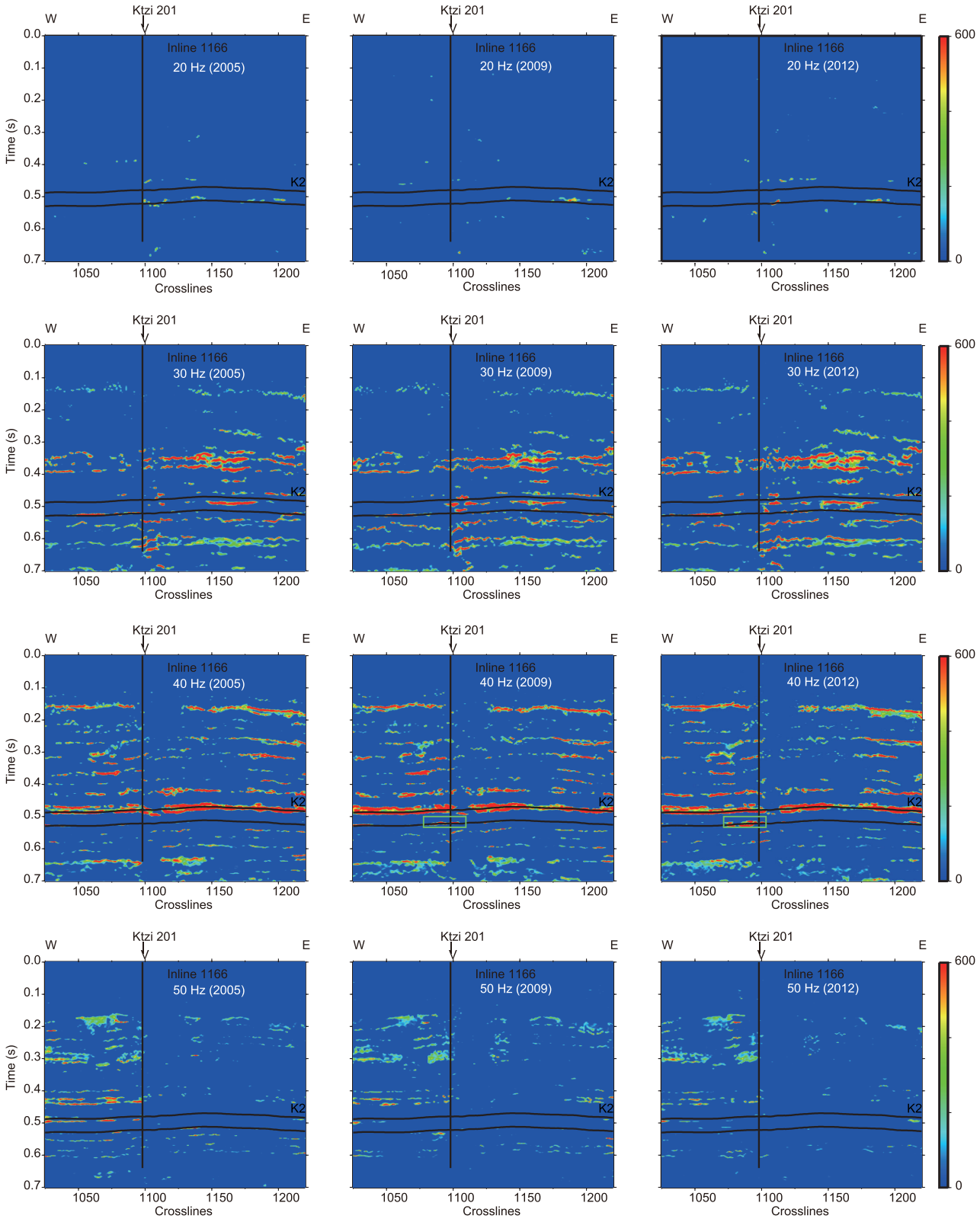

Figure 3. Reflectivity amplitude sections at discrete frequencies along inline 1166 (left-hand panel: baseline, middle: the first repeat, right-hand panel: the second repeat). The location of the injection well is marked by the black vertical line. The black horizontal lines represent the approximate locations of the K2 reflector and reservoir. Amplitude anomalies caused by the injected CO_2 are outlined by the green rectangle.

wavelet phase maps in the 2009 and 2012 surveys, one can identify that the phase of the main anomaly area concentrated around the injection well, which corresponds to the area of the injected CO_2 plume, ranges from 110° to 160°, whereas the phases outside of the main anomaly area have different values. The arch-shaped anomaly in the southwest may be an indication of the presence of sandstone channels in the floodplain facies of the Stuttgart Formation or due to ambient noise. The anomalies observed in the northwest corner and

Downloaded from http://gji.oxfordjournals.org/ at Bibliothek des Wissenschaftsparks Albert Einstein on September 19, 2016

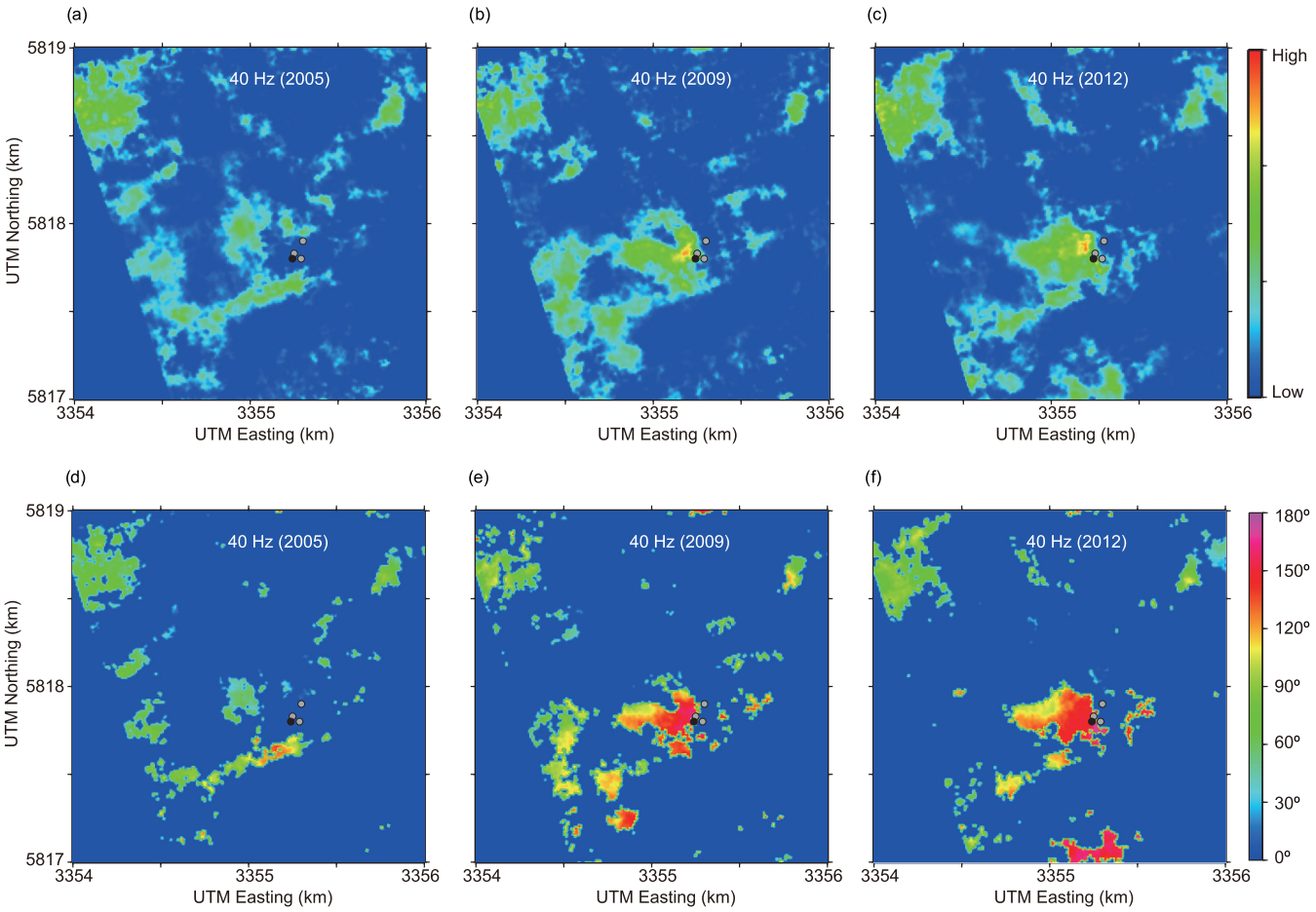

Figure 4. 40 Hz horizon maps of reflectivity amplitude (top panel) and wavelet phase (bottom panel, after Huang *et al*. 2016) at the reservoir level. From left to right: baseline, the first repeat and second repeat. The locations of the injection well and three observation wells are marked by the black and grey dots, respectively.

along the road south of the site can be correlated with the relatively high noise of local traffic due to several trucks passing between Etzin and Neu Falkenrehde (Huang *et al*. 2016). The patchy anomaly in the northeast corner can be linked to the wind turbines field that has been identified as a source of seismic noise in Gassenmeier *et al*. (2015). These maps also show the challenge of monitoring CO_2 sequestration using active seismic: CO_2 storage sites will generally be near the emission sources (large industrial areas), making the anthropogenic noise something unavoidable to work with. Fig. 5 shows the corresponding reflectivity amplitude difference maps in comparison with the previous normalized time-lapse amplitude difference maps at the reservoir level. After subtracting, the footprint attributed to the local traffic significantly decreases. The sandstone channels recognized in the first repeat are more obvious than for the second repeat. This may be due to the higher signal-to-noise ratio present in this area of the first repeat based on previous analyses of ambient noise (Kashubin *et al*. 2011; Huang *et al*. 2016). Compared to the main extent of the seismic amplitude difference, the majority of the reflectivity amplitude difference displays a similar outline and trend of CO_2 migration. In addition, the anomaly is more concentrated around the injection well. This is probably due to the complex spectral decomposition method being less sensitive to ambient noise. By combining the results of the monochromatic reflectivity amplitude and the seismic amplitude maps, the risk of misinterpreting CO_2 anomalies, corresponding to CO_2 migration, can be reduced.

3 QUANTITATIVE CO_2 EVALUATION UTILIZING TUNING FREQUENCY

3.1 Thickness determination

The net reservoir at the Ketzin site can be classified as a thin layer, since the thickness of the primary sandstone channels in the upper part of the Stuttgart Formation, ranging from 9 to 20 m (Förster *et al*. 2010), is less than 1/4 of the dominant wavelength. It is challenging to determine the thickness of a thin reservoir using seismic reflections in the time domain. According to Partyka *et al*. (1999), the two-way temporal thickness t of the layer is a function of the period of the amplitude spectrum in the frequency domain P_f, namely $t = 1/P_f = 1/2f$, where f is the first tuning frequency. The amplitude spectrum of the thin layer can be constructed by transforming the reflection seismic data within the zone of the reservoir layer from the time domain to the frequency domain. However, for field data, normally it is not easy to entirely separate one reflection from the other in the time domain, especially when these are in close vicinity to each other. In order to minimize the truncation errors due to windowing (Hall 2006), we make use of the reflectivity amplitude data produced by the complex spectral decomposition method instead of the reflection seismic data. As shown earlier, this is because the reflectivity amplitude with its higher time–frequency resolution can more accurately delineate the zone of the reservoir without including the other reflections. The discrete-frequency reflectivity amplitude

Downloaded from http://gji.oxfordjournals.org/ at Bibliothek des Wissenschaftsparks Albert Einstein on September 19, 2016

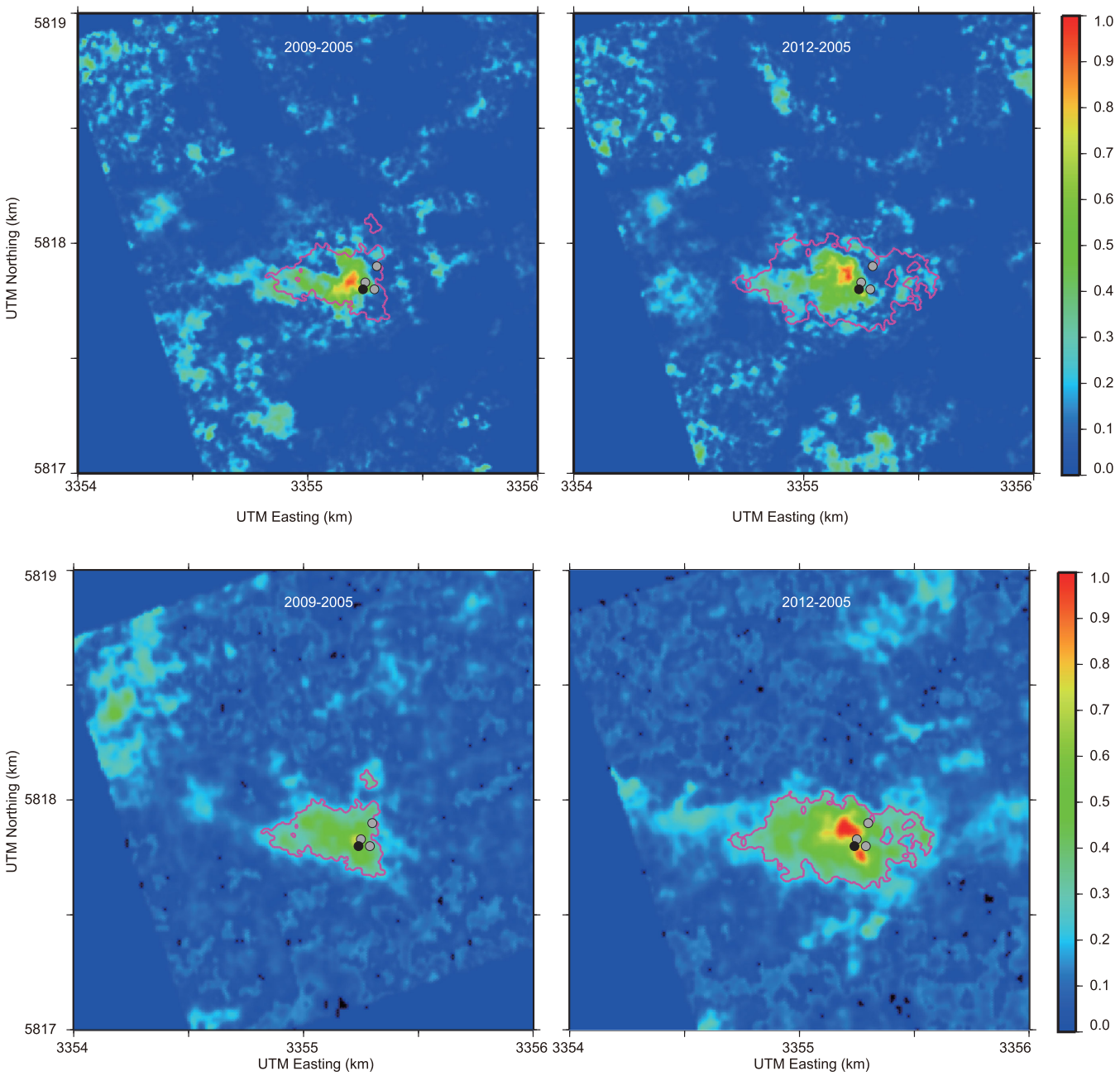

Figure 5. Normalized time-lapse difference maps at the reservoir level. Top panel: reflectivity amplitude difference of 40 Hz, bottom panel: seismic amplitude difference after Ivandic *et al*. (2015). The seismic amplitude difference is outlined by the magenta contour line at the 0.25 level. This contour is plotted on the reflectivity amplitude maps. The locations of the injection well and three observation wells are marked by the black and grey dots, respectively.

data in the temporal window that includes the reservoir zone are then transformed into the frequency domain. After multiplying the corresponding amplitude spectrum of the Ricker wavelet in the complex wavelet library and summing all the discrete-frequency amplitude spectra, the amplitude spectrum of the thin layer is constructed. Source wavelet overprint, noise and thin-bed interference, which is the component of interest, constitute the amplitude spectrum (Partyka *et al*. 1999). In order to extract the tuning frequency from the thin-bed interference pattern, the effect of the band-limited wavelet can be minimized by scaling the amplitude spectrum according to the extracted wavelet.

We first calculated the layer thickness for a synthetic time-lapse case (Fig. 6). The baseline model was established according to the velocity and density data measured in the Ktzi 201 well (Norden *et al*. 2010). The yellow inverted trapezoid, which is the second layer, (Fig. 6a) represents the reservoir sandstone. The zero-offset synthetic seismic data were generated by convolution of a 40 Hz Ricker wavelet with the reflectivity series. Then, the temporal thickness of the reservoir was derived using the extracted tuning frequency. As shown in Fig. 6(b), the first tuning frequency of trace 92 is located at the frequency corresponding to the first trough of the balanced amplitude spectrum when the top and base of the reflector have the same polarity. The determined tuning frequency is 51 Hz which corresponds to the temporal thickness of 9.8 ms (in close agreement with the theoretical value 10 ms). The comparison between the real and calculated temporal thickness (Fig. 6c) illustrates that most of

Downloaded from http://gji.oxfordjournals.org/ at Bibliothek des Wissenschaftsparks Albert Einstein on September 19, 2016

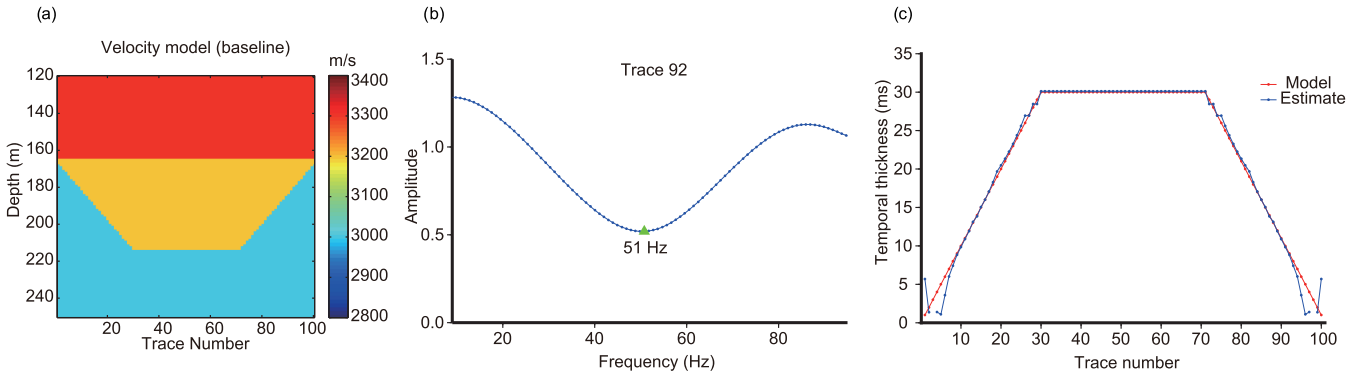

Figure 6. (a) Velocity model of baseline, (b) amplitude spectrum of trace 92 and (c) comparison of actual and determined temporal thickness. The green triangle in (b) represents the determined tuning frequency. Red and blue lines in (c) are the thickness of the actual and calculated values for the baseline model.

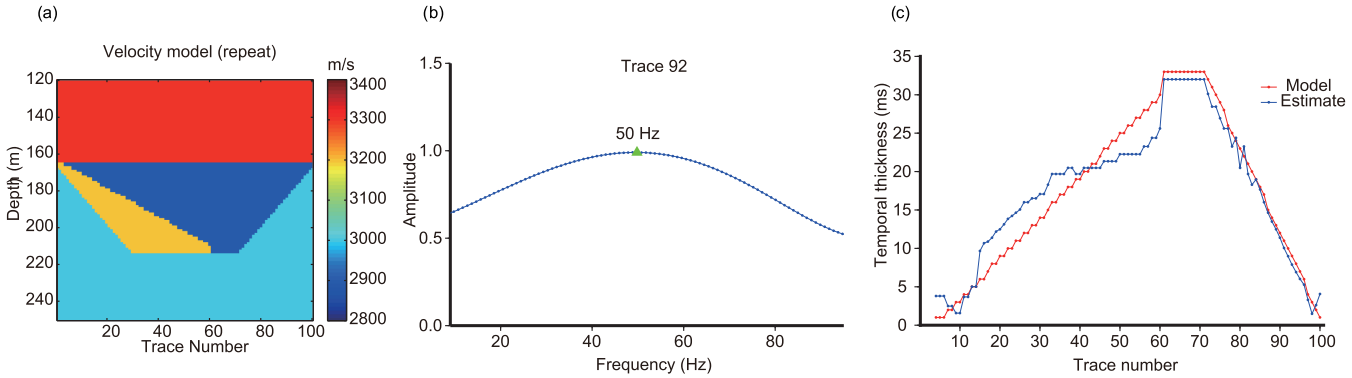

Figure 7. (a) Velocity model of repeat, (b) amplitude spectrum of trace 92 and (c) comparison of actual and determined temporal thickness. The green triangle in (b) represents the determined tuning frequency. Red and blue lines in (c) are the thickness of the actual and calculated values for the repeat model.

the temporal thicknesses of the reservoir are correctly determined. For the temporal thickness between 1 and 8 ms, the accuracy becomes less and no tuning frequency is found at 3 ms. The model after CO_2 injection is shown in Fig. 7. The presence of CO_2 produces a velocity decrease in the reservoir and forms a new layer within it. From trace 4 to 60, the reservoir is partly saturated with CO_2 while for traces 61 to 100 the reservoir is fully saturated with CO_2. After applying complex spectral decomposition to the time-lapse amplitude difference, the temporal thickness of the CO_2 plume is obtained (Fig. 7c). Note that the first tuning frequency is located at the frequency corresponding to the first peak of the balanced amplitude spectrum when the top and base of the reflector have the opposite polarity (Fig. 7b). The determined tuning frequency is 50 Hz which corresponds to the temporal thickness of 10 ms (also in reasonable agreement with the theoretical value 11 ms). Compared with the baseline result, the error between the real and calculated temporal thickness of the CO_2 plume increases, especially for the reservoir partly saturated with CO_2, due to the impact of the reservoir base. In spite of this, the error is acceptable and the calculated thickness can reflect the variation trend of the real thickness.

For the time-lapse 3-D seismic data at the Ketzin site, the source wavelet was extracted using well log information and the seismic data windowed from 200 to 800 ms around the location of the Ktzi 201 well (Huang *et al*. 2015). The amplitude spectrum of this source wavelet was then used to balance the amplitude spectrum. Due to the reservoir heterogeneity, extraction of peaks or troughs in the data is challenging, since the polarity of the reservoir top and base is unknown. An alternative approach is to (1) determine the first peak of the balanced amplitude spectrum, (2) multiply the amplitude spectrum with −1, (3) determine the first peak of the balanced amplitude spectrum multiplied by −1, and (4) choose the minimum frequency corresponding to peaks. The chosen frequency correctly corresponds to the first tuning frequency and allows mapping of the reservoir tuning frequency (Fig. 8) extracted from the baseline data. The thickness of the reservoir is inversely proportional to the tuning frequency. The mapped tuning frequency representing

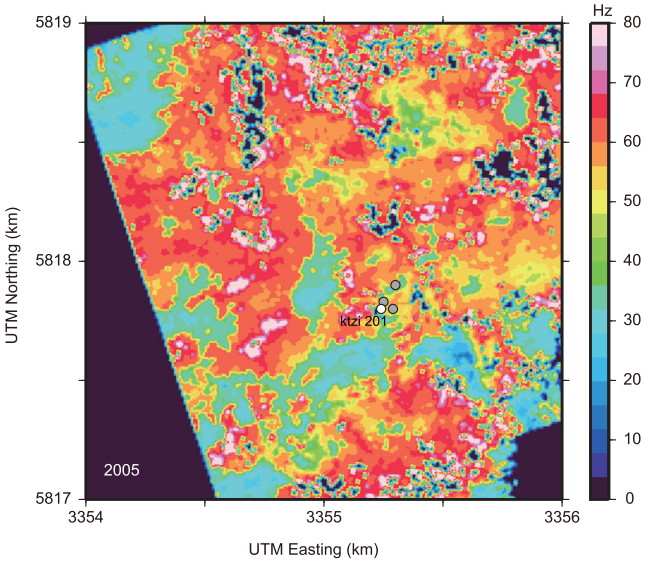

Figure 8. Reservoir tuning frequency map extracted from the baseline seismic survey. The locations of the injection well and the three observation wells are marked by the white and grey dots, respectively.

Downloaded from http://gji.oxfordjournals.org/ at Bibliothek des Wissenschaftsparks Albert Einstein on September 19, 2016

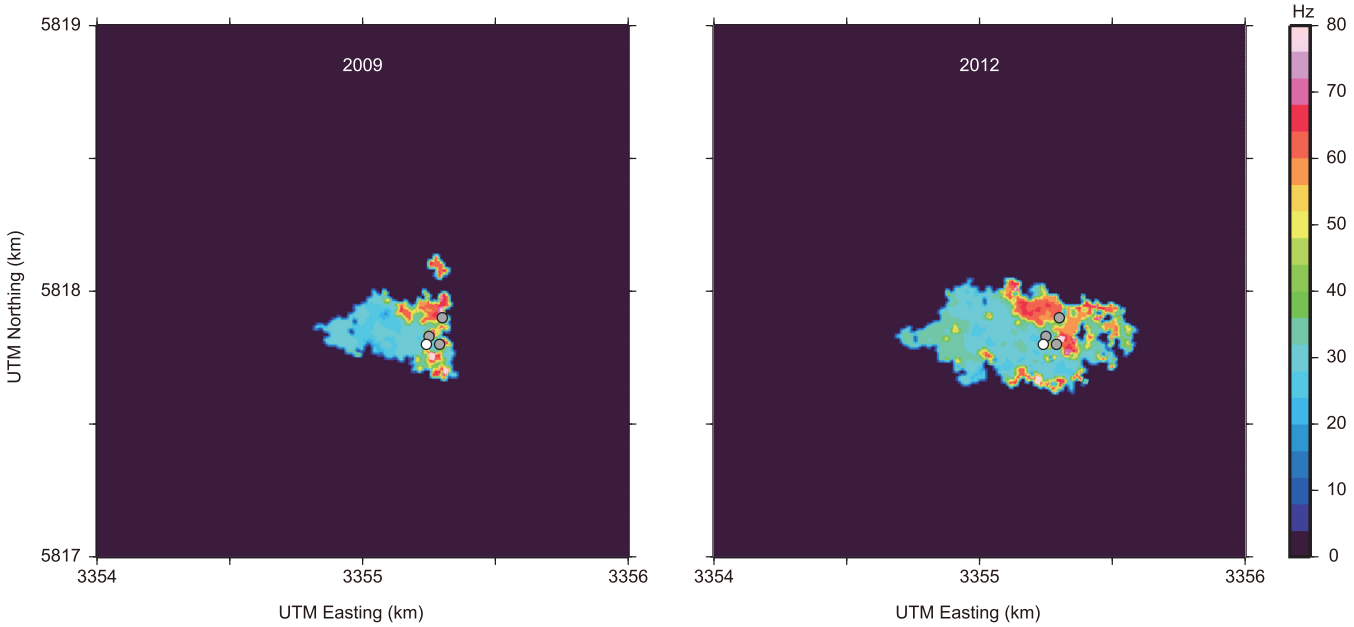

Figure 9. Tuning frequency map for the two repeat surveys. The locations of the injection well and three observation wells are marked by the white and grey dots, respectively.

the sandstone unit ranges from 50 to 80 Hz, corresponding to a two-way temporal thickness between 6.3 and 10 ms. Ultrasonic laboratory experiments indicate an average velocity of the reservoir sandstone saturated with 100 per cent formation brine at the Ketzin site of 3135 m s^{-1} (Ivanova *et al*. 2012). Therefore, the calculated thickness of the reservoir based on the tuning frequency ranges from 9.7 to 17.4 m, consistent with the 9–20 m sandstone unit derived from well logs (Förster *et al*. 2010).

Complex spectral decomposition was also applied to the normalized time-lapse amplitude differences in order to extract the tuning frequency related to the gaseous part of the CO_2 plume. A cut-off of 0.25 for the amplitude difference at the reservoir level was adopted to define the distribution of the gaseous CO_2, since values smaller than 0.25 scatter all over the map and are, consequently, regarded as ambient noise (Ivandic *et al*. 2015). Then the tuning frequencies were determined from the balanced amplitude spectra of the time-lapse amplitude differences of the reservoir layer within the defined area. Fig. 9 shows the determined tuning frequencies due to the injected CO_2. It clearly shows that the tuning frequency at the edge of the amplitude difference anomaly is comparatively high. Much higher tuning frequencies are identified in the northern, southern and eastern areas encompassing the injection well. These areas are assumed to be the low-permeability CO_2 migration pathways and are likely to explain the preferred WNW trend of the CO_2 propagation. The determined values of the tuning in the vicinities of the Ktzi 201, Ktzi 202 and Ktzi 203 wells are 27, 61 and 66 Hz, respectively, for the first repeat survey compared with 25, 59 and 29 Hz for the second one. For the Ktzi 200 well, no tuning is found for the first repeat survey, whereas a tuning frequency of 35 Hz is determined for the second repeat survey. The corresponding two-way temporal thicknesses of the gaseous CO_2 plume at these four wells in comparison with the measured thickness of the sandstone unit from well logging are given in Table 1. As shown, the temporal thickness of the gaseous CO_2 plume increases with increasing amounts of injected CO_2. For the second repeat survey, the temporal thickness variation of the gaseous CO_2 plume agrees well with the thickness variation of the reservoir sandstone. A significant increase in the temporal thickness of the gaseous CO_2 plume is observed at Ktzi 203. This indicates a preferential migration of the gaseous CO_2 plume in the up-dip direction, which is in agreement with observations from the other seismic (Ivandic *et al*. 2012) and electromagnetic methods (Bergmann *et al*. 2012; Grayver *et al*. 2014) employed at the Ketzin site. It is known that the velocity of the sandstone after CO_2 injection is influenced by the CO_2 saturation. The average velocity of the reservoir sandstone containing CO_2 is around 2370 m s^{-1} based on an average CO_2 saturation of 50 per cent measured at Ktzi 201 (Ivanova *et al*. 2013b). Using $H = VT/2$, where V is reservoir velocity and T is the two-way temporal thickness, the corresponding thicknesses (H) of the gaseous CO_2 plume at the two repeat times at the Ktzi 201 well correspond to 21.7 and 23.3 m, both close to the net thickness of the reservoir sandstone but slightly higher. This is reasonable since pulsed neutron-gamma logging had detected the presence of CO_2 within a thinner siltstone and sandstone layer underlying the main injection interval in the Ktzi 201 well (Ivanova *et al*. 2012; Baumann *et al*. 2014).

Table 1. Thickness of the reservoir sandstone compared with calculated temporal thickness of the gaseous CO_2 plume.

Well	Reservoir sandstone (m)	Gaseous CO_2 plume (ms)	
		1st repeat	2nd repeat
Ktzi 200	16	–	14.2
Ktzi 201	19	18.3	19.7
Ktzi 202	9	8.3	8.5
Ktzi 203	18	7.5	17.1

3.2 Evaluation of CO_2 saturation and pressure based anomalies

Time-lapse amplitude variation with offset (AVO) analysis has been used to discriminate between pressure and saturation changes caused by CO_2 injection (Landrø 2001). Landrø *et al*. (2003) exploited AVO to estimate pressure and saturation changes from marine multicomponent time-lapse seismic data. Grude *et al*. (2013)

Downloaded from http://gji.oxfordjournals.org/ at Bibliothek des Wissenschaftsparks Albert Einstein on September 19, 2016

used a first order approximation to discriminate the pressure effect from the saturation effect. However, analysis of AVO may be invalid, if thin-layer interference occurs (Swan 1991; Juhlin & Young 1993; Chadwick *et al*. 2010). At the Ketzin site, Ivanova *et al*. (2013a) investigated these two effects using the modelled AVO response and concluded that it is difficult to discriminate between these two effects in the field data due to the limited signal-to-noise ratio and reservoir heterogeneity.

The effective stress in the formation decreases with increasing pore pressure due to CO_2 injection. Consequently, *P*-wave velocity decreases and noticeable changes in the seismic response similar to those triggered by CO_2 saturation may be detected. Note that a reduced *S*-wave velocity will also be the result of increased pore pressure. Such a reduction will not occur, if the *P*-wave velocity reduction is only related to saturation effects. An analysis of the tuning frequency may allow for discrimination of pressure and saturation effects if *S*-wave velocity information is not available for the reservoir. Increased pore pressure will affect the entire reservoir height and the resulting tuning frequency will generally be lower than that due to saturation, since the gaseous CO_2 saturation will normally be concentrated to the upper portion of the reservoir (White *et al*. 2015). Utilizing these distinct tuning frequencies, the anomalies generated by pressure and gaseous CO_2 saturation can potentially be separated from each other. Using sandstone thicknesses determined from the baseline survey, the corresponding tuning frequencies for the sandstone thicknesses fully saturated with CO_2 were calculated from the model in Section 3.1. These calculated tuning frequencies are assumed to be theoretical lower limits of the repeat tuning frequencies and therefore are set as cut-off values for the repeat surveys to distinguish between saturation and pressure anomalies. If the repeat tuning frequency is lower than the cut-off, it is because pressure effects overcome the saturation effect, and vice versa. The anomaly discrimination between pressure and CO_2 saturation effects is mapped in Fig. 10. A stronger pressure anomaly is observed in the first repeat survey compared to the second repeat survey. This is consistent with the higher downhole pressure measured during the first repeat, while a noticeable decrease in downhole pressure was recorded during the second repeat (Martens *et al*. 2014). As expected, the outline of the gaseous CO_2 extent increases in size as more CO_2 is injected.

3.3 Assessment of CO_2 mass

Quantitative assessment of the CO_2 mass is an important component in monitoring the growth of the gaseous CO_2 distribution and any potential leakage (Arts *et al*. 2004b; Chadwick *et al*. 2005; Lüth *et al*. 2015). Previously, the assessment of the CO_2 mass at the Ketzin pilot site was based on the time delays from seismic reflections below the reservoir and the reflection strength of the CO_2 induced seismic anomaly. As discussed earlier, the CO_2 evaluation utilizing the determined tuning frequency extracted by the complex spectral decomposition can recognize the thickness of the thin layer and is independent of the seismic phase compared with the methods using time delays. In addition, the gaseous CO_2 mass can be derived from the anomaly resulting from CO_2 saturation without including the anomaly caused by pressure.

The following equation (Arts *et al*. 2002) can be used to calculate the mass of the CO_2:

$$M_{CO_2} = \sum_{i=1}^{N} \rho_i \cdot S_i \cdot \phi_i \cdot H_i \cdot \mathrm{d}x \cdot \mathrm{d}y, \quad (1)$$

where N is the number of CDP bins, ρ_i and S_i are the density and saturation of the CO_2 in the ith CDP bin, ϕ is the porosity of the reservoir sandstone, H is the thickness of the gaseous CO_2, dx and dy determine the CDP bin size (12 m × 12 m). H can be calculated using $H = V_g T_g/2$, where T_g is the thickness of gaseous CO_2 derived from the time-lapse 3-D surveys and V_g is the velocity in the reservoir saturated with CO_2.

However, it is impractical to directly acquire real and detailed values from the reservoir containing CO_2, due to the highly heterogeneous lithology and the generally limited understanding of the subsurface. Detailed velocities at two repeat times and porosities previously built by incorporating logging data, interpretation of 3-D seismic data and history-matched dynamic flow simulations (Kempka *et al*. 2013; Norden & Frykman 2013; Huang *et al*. 2015) were used to represent the corresponding values of the reservoir saturated with CO_2. Detailed parameters about density and CO_2 saturation were extracted from the dynamic flow simulations (Kempka *et al*. 2013; Class *et al*. 2015). Fig. 11 shows the distribution of the CO_2 mass calculated using H from the field data and the other parameters from the dynamic simulations. It is clearly seen that more CO_2 is present around the injection well, while less CO_2 is present at the boundaries of the gaseous CO_2 extent. The calculated CO_2 masses for the two repeat times are 22.0 and 45.1 kt, compared to the actual injected masses of 23.5 and 61 kt, respectively. The discrepancy between the injected and calculated CO_2 amount is partly attributed to the uncertainty in reservoir properties. Therefore, it is necessary to investigate the impact of different parameters on assessment of CO_2 mass. Different combinations of parameters were tested and are shown in Table 2. The constant velocity of 3000 m s^{-1} for the two repeat times is the average value of the detailed velocities. The average porosity of 20 per cent was obtained from core analysis (Förster *et al*. 2010). The calculated CO_2 densities of 266.62 and 215 kg m^{-3} are based on observed average temperatures and pressures in the wells at the two repeat times, respectively. It can be seen that the amplitude cut-off has significant influence on the results of the calculated CO_2 mass, whereas using average or detailed reservoir parameters only slightly affects it. An increase of 0.05 in amplitude cut-off corresponds to a 15–25 per cent reduction in calculated mass. By using the values of 0.3 and 0.2 for amplitude cut-off, the lower and upper limits of the calculated CO_2 mass were determined, namely 16.6 and 26.4 kt for the first repeat time and 38.6 and 63.1 kt for the second repeat time.

4 DISCUSSION

Continuous layers with greater vertical resolution are clearly seen in the reflectivity amplitude sections extracted from the original seismic data via the trace-by-trace complex spectral decomposition method. Experienced geophysicists can interpret the formations based on the seismic reflection data. However, by combining the reflectivity amplitude data with conventional seismic data, it is easier to recognize the top and base of the formations and reduce the risk of biased interpretations. The discontinuity found east and south of the injection site is consistent with the expected reservoir heterogeneity and can be used to explain why the gaseous CO_2 prefers to move WNW.

The synthetic example verifies that the calculated temporal thickness is accurate for the baseline model and the layer fully saturated with CO_2. For the layer partly saturated with CO_2, the calculated thickness of the gaseous CO_2 generally yields acceptable results and coincides with its theoretical thickness changes. The increase

Downloaded from http://gji.oxfordjournals.org/ at Bibliothek des Wissenschaftsparks Albert Einstein on September 19, 2016

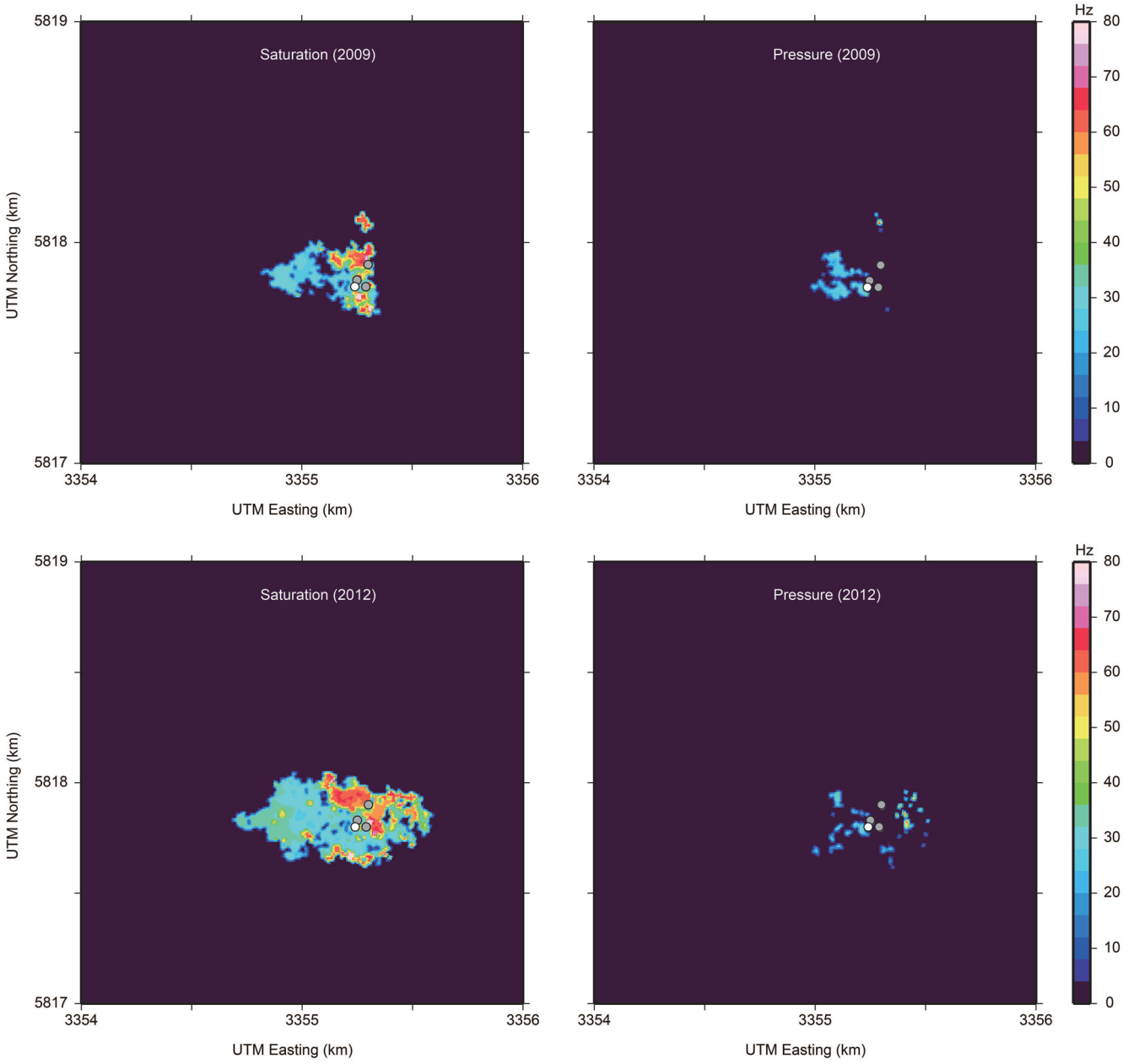

Figure 10. Anomaly maps of apparent pressure and CO_2 saturation for the two repeat surveys. Top panel: the first repeat survey, bottom panel: the second repeat survey. The locations of the injection well and three observation wells are marked by the white and grey dots, respectively.

in error originates from the influence of the layer base. This implies that the determined temporal thickness of the thin layer becomes less accurate if a neighbouring thin layer is present.

Abnormally high tuning frequencies in the northern, southern and eastern areas around the injection well are likely to imply low permeability or poor connectivity in those locations. This is also consistent with the observed predominant trend of CO_2 growth to WNW. Analysis of the amplitude anomaly for discrimination of pressure versus CO_2 saturation using the extracted tuning frequency shows that a pressure effect is present, but is not extensive at the Ketzin site. Most of the anomaly is due to CO_2 saturation. This suggests that connected sandstone channels exist in the reservoir, predominantly towards the west and north of the injection location.

CO_2 mass assessment was performed based on the tuning frequency interpretation of the CO_2 saturation. This approach eliminates the pressure effect and is not influenced by the seismic phase when evaluating the CO_2 mass. However, uncertainties remain in the CO_2 mass assessment. Apart from reservoir heterogeneity and limited knowledge on the subsurface, ambient noise is another possible factor affecting uncertainties although the range of the gaseous CO_2 plume was defined by using a cut-off of 0.25 for the amplitude difference to exclude noise. In addition, exact wavelet extraction using the balanced amplitude spectrum is also important to correctly determine the tuning frequency. The previous estimates using time delays to assess CO_2 mass at Ketzin had two main uncertainties, the time-delay cut-off and the amplitude cut-off, whereas the amplitude cut-off is the main uncertainty factor in mass assessment when using the tuning frequency approach. Assumptions concerning the reservoir parameters have a limited influence on the uncertainty of the CO_2 mass assessment. In addition to the above factors, the

Downloaded from http://gji.oxfordjournals.org/ at Bibliothek des Wissenschaftsparks Albert Einstein on September 19, 2016

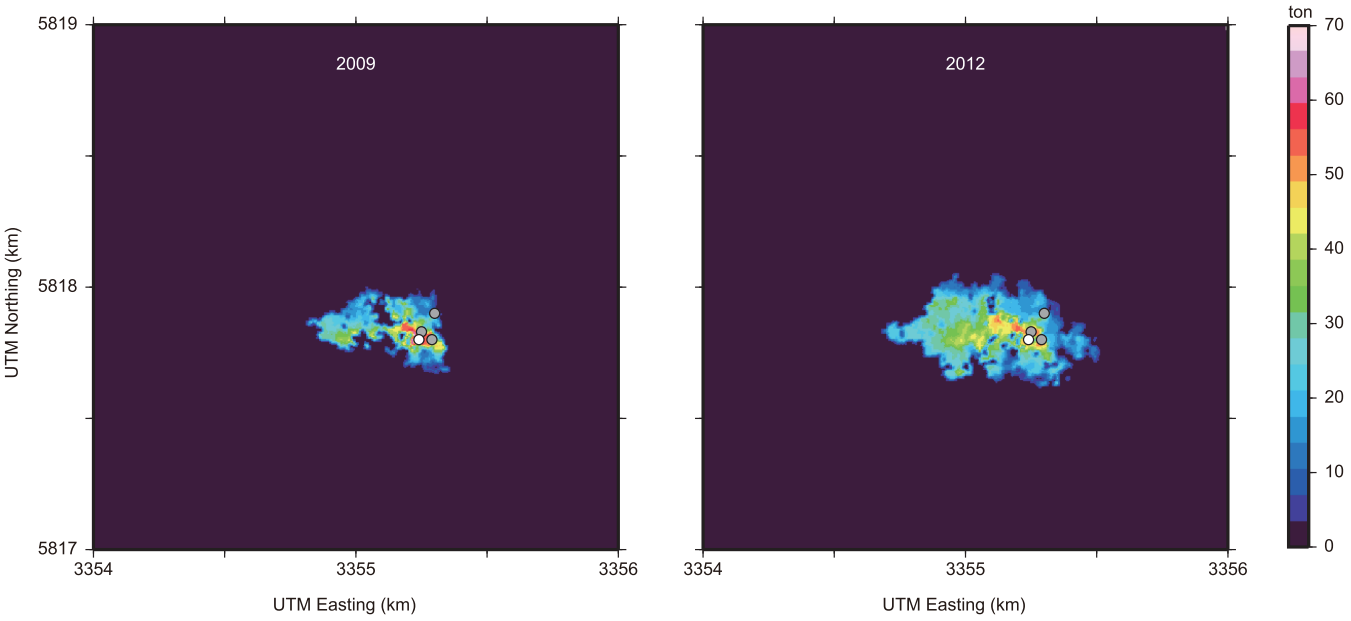

Figure 11. Distribution of the calculated CO_2 mass for the two repeat surveys. The locations of the injection well and three observation wells are marked by the white and grey dots, respectively.

Table 2. Comparison of calculated CO_2 mass using different parameters. Approximately 23.5 and 61 kt of CO_2 were injected at the two repeat times.

Amplitude cut-off	Velocity (m s^{-1})	Porosity (%)	CO_2 density (kg m^{-3})		Calculated mass (kt)	
			1st repeat	2nd repeat	1st repeat	2nd repeat
0.25	Detailed	Detailed	Detailed	Detailed	22.0	45.1
0.25	Detailed	20	Detailed	Detailed	21.6	45.8
0.25	Detailed	Detailed	266.62	215	21.1	46.2
0.25	Detailed	20	266.62	215	21.1	46.9
0.25	3000	20	266.62	215	21.2	48.0
0.3	Detailed	Detailed	Detailed	Detailed	18.4	38.6
0.3	Detailed	20	266.62	215	16.6	39.1
0.2	Detailed	Detailed	Detailed	Detailed	26.3	57.8
0.2	Detailed	20	266.62	215	26.4	63.1

relatively high CO_2 dissolution ratio, about 25 per cent as derived from the dynamic simulations at the relevant times, may also contribute to the mass discrepancy. High dissolution rates are reasonable given the structural heterogeneity of the Stuttgart Formation (sand channels resulting in a large CO_2-brine interface) and the relatively low injection rates.

Using parameters from the dynamic simulations and 0.25 for the amplitude cut-off, the calculated CO_2 masses for the two repeat times are 22.0 and 45.1 kt, which are 7 and 26 per cent less than the actual injected masses, respectively. Assuming CO_2 dissolution accounts for a decrease of 25 per cent for both repeat surveys, it can be seen that the mass of injected CO_2 for the first repeat survey was significantly overestimated whereas the mass of injected CO_2 for the second repeat survey was slightly underestimated. There are at least two possible explanations for this. First, for the comparatively thin layer partly saturated with CO_2, the determined temporal thickness of CO_2 from the repeat model is larger than the theoretical temporal thickness of CO_2 (Fig. 7c) due to the influence of the layer base. This will lead to an increase of the estimated CO_2 mass. Second, some thin layers of CO_2 at the margins of the main area of the CO_2 plume were excluded after applying the amplitude cut-off. This will lead to a decrease of the estimated CO_2 mass. Assuming a simple case with a number of constant-thickness thin layers partly saturated

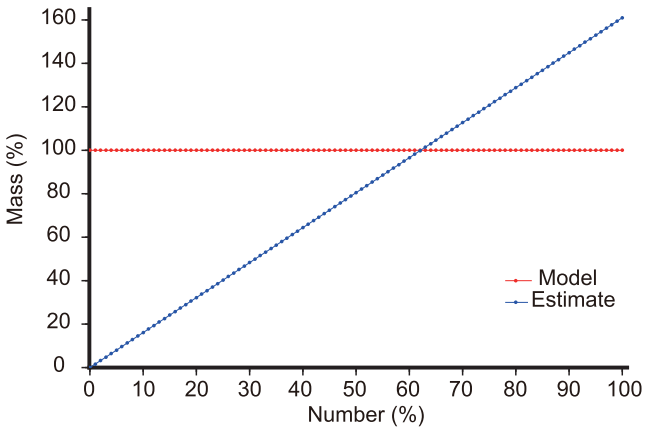

Figure 12. Comparison of the total amount of the CO_2 and the estimated amount of the CO_2 with percentage of the thin layers used.

with constant-thickness thin CO_2 layers (e.g. trace 16 in Fig. 7a), the relationship between the total amount of the CO_2 within these thin layers and the estimated amount of the CO_2 for a given percentage of used thin layers is shown in Fig. 12. It is clearly shown that if the percentage of the thin layers used to estimate CO_2 mass is less

Downloaded from http://gji.oxfordjournals.org/ at Bibliothek des Wissenschaftsparks Albert Einstein on September 19, 2016

than a certain point (62 per cent), the estimated CO_2 mass is underestimated while if the percentage exceeds the point, the estimated CO_2 mass is overestimated. This implies that in comparison with the first repeat survey, more thin layers saturated with CO_2 were excluded from the second repeat survey after applying the same amplitude cut-off of 0.25. This is reasonable since the areal extent of thin layers saturated with CO_2 in the second repeat time should be larger than that at the first repeat time due to the process of CO_2 diffusion (thin layer spreading). In addition, at some locations CO_2 saturation and pressure may generate very similar responses, which are impossible to distinguish using the tuning frequency. This may also contribute to increases in the estimated CO_2 mass.

5 CONCLUSIONS

Compared with conventional spectral decomposition methods constrained by the uncertainty principle, the complex spectral decomposition method provides higher time–frequency resolution and is less sensitive to random noise. This frequency-dependent information was used for analysis of the thin reservoir and the gaseous CO_2 extent at the Ketzin pilot site. The reflectivity amplitude sections exhibit higher temporal resolution and more stratigraphic details compared to the original seismic data. The observed anomaly distribution at a dominant frequency of 40 Hz is consistent with previous time-lapse amplitude difference results. The tuning frequency maps reflect the temporal thickness variation of the reservoir sandstone and gaseous CO_2. The tuning frequency analysis allows the effects of CO_2 saturation to be separated from pressure effects, providing a quantitative evaluation of the non-dissolved CO_2 mass in the reservoir.

However, significant uncertainty remains in the mass assessment due to the presence of ambient noise, errors in determining the tuning frequency, reservoir heterogeneity, a limited understanding of the complex subsurface and limited validation options for assessing the amount of CO_2 dissolution actually occurring in the Stuttgart Formation as derived from dynamic simulations. These factors are considered as the main reasons for the discrepancy between the injected and calculated CO_2 mass. A combined approach using seismic and other geophysical methods may contribute to a decrease in uncertainties. Given that the electromagnetic method is also very sensitive to the presence of injected CO_2 due to the resistivity contrast (Grayver *et al*. 2014; Bergmann *et al*. 2015), 4-D joint seismic-electromagnetic monitoring for the injected CO_2 plume can potentially be used to improve coverage and provide useful complementary information on the CO_2 distribution.

ACKNOWLEDGEMENTS

Part of this work was conducted within the CO_2MAN and COMPLETE collaborative projects that facilitated research and development work at the Ketzin pilot site and was supported by the German Federal Ministry of Education and Research (BMBF) and the industry partners VNG, RWE Power AG, Vattenfall, Statoil Petroleum AS, Dillinger Hüttenwerke, Saarstahl AG and OMV Exploration and Production GmbH. GLOBE Claritas™ under license from the Institute of Geological and Nuclear Sciences Limited, Lower Hutt, New Zealand was used to process the seismic data. Hampson and Russell (CGG Veritas) provided Pro4D for the time lapse analysis. Fei Huang would like to thank the China Scholarship Council for providing him with a scholarship for his PhD studies. Fengjiao Zhang would like to thank the National Natural Science Foundation of China (grant number 41404092) for partly supporting the work. Finally, we thank the editor and one anonymous reviewer for their constructive comments that helped to improve this paper.

REFERENCES

Arts, R. & Eyvazi, F.J., 2011. Monitoring and modelling CO_2 injection at Sleipner, in *Proceedings of the 73rd EAGE Conference and Exhibition-Workshops 2011*, EAGE Extended Abstract, Vienna, Austria, doi:10.3997/2214-4609.20144723.

Arts, R., Elsayed, R., Van Der Meer, L., Eiken, O., Ostmo, S., Chadwick, A., Kirby, G. & Zinszner, B., 2002. Estimation of the mass of injected CO_2 at Sleipner using time-lapse seismic data, in *Proceedings of the 64th EAGE Conference and Exhibition*, EAGE Expanded Abstract H-16, Florence, Italy.

Arts, R., Eiken, O., Chadwick, A., Zweigel, P., van der Meer, B. & Kirby, G., 2004a. Seismic monitoring at the Sleipner underground CO_2 storage site (North Sea), *Geol. Soc., Lond., Spec. Pub.*, **233**(1), 181–191.

Arts, R., Eiken, O., Chadwick, A., Zweigel, P., van der Meer, L. & Zinszner, B., 2004b. Monitoring of CO_2 injected at Sleipner using time-lapse seismic data, *Energy*, **29**(9–10), 1383–1392.

Baumann, G., Henninges, J. & De Lucia, M., 2014. Monitoring of saturation changes and salt precipitation during CO_2 injection using pulsed neutron-gamma logging at the Ketzin pilot site, *Int. J. Greenhouse Gas Contl.*, **28**, 134–146.

Beck, A. & Teboulle, M., 2009. A fast iterative shrinkage-thresholding algorithm for linear inverse problems, *SIAM J. Imaging Sci.*, **2**(1), 183–202.

Bergmann, P., Schmidt-Hattenberger, C., Kiessling, D., Rücker, C., Labitzke, T., Henninges, J., Baumann, G. & Schütt, H., 2012. Surface-downhole electrical resistivity tomography applied to monitoring of CO_2 storage at Ketzin, Germany, *Geophysics*, **77**(6), B253–B267.

Bergmann, P. *et al.*, 2015. Towards 4D Joint Inversion for Subsurface Monitoring-Synthetic Study in the Context of the Ketzin CO_2 Storage Site, in *Proceedings of the Third Sustainable Earth Sciences Conference and Exhibition*, Celle, Germany.

Bonar, D., Sacchi, M.D., Cao, H. & Li, X.-G., 2010. Time-frequency analysis via deconvolution with sparsity constraints, in *Proceedings of the GeoCanada*, Expanded Abstract, Calgary, Canada.

Bonar, D.C. & Sacchi, M.D., 2010. Complex spectral decomposition via inversion strategies, in *Proceedings of the 80th SEG Annual Meeting*, SEG Expanded Abstract, Denver, USA, pp. 1408–1412.

Chadwick, R., Arts, R., Eiken, O., Kirby, G., Lindeberg, E. & Zweigel, P., 2004. 4D seismic imaging of an injected CO_2 plume at the Sleipner Field, Central North Sea, *Geol. Soc., Lond., Memoirs*, **29**(1), 311–320.

Chadwick, R., Arts, R. & Eiken, O., 2005. 4D seismic quantification of a growing CO_2 plume at Sleipner, North Sea, in *Proceedings of the 6th Petroleum Geology Conference*, Geological Society London, pp. 1385–1399

Chadwick, R., Noy, D., Arts, R. & Eiken, O., 2009. Latest time-lapse seismic data from Sleipner yield new insights into CO_2 plume development, *Energy Procedia*, **1**(1), 2103–2110.

Chadwick, A. *et al.*, 2010. Quantitative analysis of time-lapse seismic monitoring data at the Sleipner CO_2 storage operation, *Leading Edge*, **29**(2), 170–177.

Class, H., Mahl, L., Ahmed, W., Norden, B., Kühn, M. & Kempka, T., 2015. Matching pressure measurements and observed CO_2 arrival times with static and dynamic modelling at the Ketzin storage site, *Energy Procedia*, **76**, 623–632.

Förster, A. *et al.*, 2010. Reservoir characterization of a CO_2 storage aquifer: the Upper Triassic Stuttgart Formation in the Northeast German Basin, *Mar. Pet. Geol.*, **27**(10), 2156–2172.

Gabor, D., 1946. Theory of communication. Part 1: The analysis of information, *J. Inst. Electr. Eng. - Part III: Radio Commun. Eng,*, **93**(26), 429–441.

Downloaded from http://gji.oxfordjournals.org/ at Bibliothek des Wissenschaftsparks Albert Einstein on September 19, 2016

Gassenmeier, M., Sens-Schönfelder, C., Delatre, M. & Korn, M., 2015. Monitoring of environmental influences on seismic velocity at the geological storage site for CO_2 in Ketzin (Germany) with ambient seismic noise, *Geophys. J. Int.*, **200**(1), 524–533.

Ghaderi, A. & Landrø, M., 2009. Estimation of thickness and velocity changes of injected carbon dioxide layers from prestack time-lapse seismic data, *Geophysics*, **74**(2), O17–O28.

Grayver, A.V., Streich, R. & Ritter, O., 2014. 3D inversion and resolution analysis of land-based CSEM data from the Ketzin CO_2 storage formation, *Geophysics*, **79**(2), E101–E114.

Grude, S., Landrø, M. & Osdal, B., 2013. Time-lapse pressure–saturation discrimination for CO_2 storage at the Snøhvit field, *Int. J. Greenhouse Gas Contl.*, **19**, 369–378.

Hall, M., 2006. Resolution and uncertainty in spectral decomposition, *First Break*, **24**(12), 43–47.

Han, L., Liu, C. & Yuan, S., 2015. Can we use wavelet phase change due to attenuation for hydrocarbon detection?, in *Proceedings of the 85th SEG Annual Meeting*, SEG Expanded Abstract, Las Vegas, USA, pp. 2962–2966.

Huang, F., Juhlin, C., Kempka, T., Norden, B. & Zhang, F., 2015. Modeling 3D time-lapse seismic response induced by CO_2 by integrating borehole and 3D seismic data—a case study at the Ketzin pilot site, Germany, *Int. J. Greenhouse Gas Contl.*, **36,** 66–77.

Huang, F. *et al.*, 2016. Feasibility of utilizing wavelet phase to map the CO_2 plume at the Ketzin pilot site, Germany, *Geophys. Prospect.*, in press, doi:10.1111/1365-2478.12383.

Ivandic, M., Yang, C., Lüth, S., Cosma, C. & Juhlin, C., 2012. Time-lapse analysis of sparse 3D seismic data from the CO_2 storage pilot site at Ketzin, Germany, *J. appl. Geophys.*, **84**, 14–28.

Ivandic, M. *et al.*, 2015. Geophysical monitoring at the Ketzin pilot site for CO_2 storage: new insights into the plume evolution, *Int. J. Greenhouse Gas Contl.*, **32**, 90–105.

Ivanova, A., Kashubin, A., Juhojuntti, N., Kummerow, J., Henninges, J., Juhlin, C., Lüth, S. & Ivandic, M., 2012. Monitoring and volumetric estimation of injected CO_2 using 4D seismic, petrophysical data, core measurements and well logging: a case study at Ketzin, Germany, *Geophys. Prospect.*, **60**(5), 957–973.

Ivanova, A. & Bergmann, P.,Kummerow, J., Yang, C., Lüth, S. & Juhlin, C., 2013a. Seismic modeling of the AVO/AVA response to CO_2 injection at the Ketzin Site, Germany, *Energy Procedia*, **40**, 490–498.

Ivanova, A., Juhlin, C., Lengler, U., Bergmann, P., Lüth, S. & Kempka, T., 2013b. Impact of temperature on CO_2 storage at the Ketzin site based on fluid flow simulations and seismic data, *Int. J. Greenhouse Gas Contl.*, **19**(0), 775–784.

Johansson, T.B., Patwardhan, A.P., Nakićenović, N. & Gomez-Echeverri, L., 2012. *Global Energy Assessment: Toward a Sustainable Future*, Cambridge Univ. Press.

Juhlin, C. & Young, R., 1993. Implications of thin layers for amplitude variation with offset (AVO) studies, *Geophysics*, **58**(8), 1200–1204.

Juhlin, C. *et al.*, 2007. 3D baseline seismics at Ketzin, Germany: the CO_2SINK project, *Geophysics*, **72**(5), B121–B132.

Kashubin, A., Juhlin, C., Malehmir, A., Lüth, S., Ivanova, A. & Juhojuntti, N., 2011. A footprint of rainfall on land seismic data repeatability at the CO_2 storage pilot site, Ketzin, Germany, in *Proceedings of the 81st SEG Annual Meeting*, SEG Expanded Abstract, San Antonio, USA, pp. 4165–4169.

Kazemeini, S.H., Juhlin, C., Zinck-Jørgensen, K. & Norden, B., 2009. Application of the continuous wavelet transform on seismic data for mapping of channel deposits and gas detection at the CO_2SINK site, Ketzin, Germany, *Geophys. Prospect.*, **57**(1), 111–123.

Kempka, T., Klein, E., De Lucia, M., Tillner, E. & Kühn, M., 2013. Assessment of long-term CO_2 trapping mechanisms at the Ketzin pilot site (Germany) by coupled numerical modelling, *Energy Procedia*, **37**, 5419–5426.

Landrø, M., 2001. Discrimination between pressure and fluid saturation changes from time-lapse seismic data, *Geophysics*, **66**(3), 836–844.

Landrø, M., Veire, H.H., Duffaut, K. & Najjar, N., 2003. Discrimination between pressure and fluid saturation changes from marine multicomponent time-lapse seismic data, *Geophysics*, **68**(5), 1592–1599.

Liebscher, A. & Münch, U., 2015, eds. *Geological Storage of CO_2— Long Term Security Aspects*, GEOTECHNOLOGIEN Science Report No. 23, Springer.

Liu, C., Han, L., Zhang, Y. & Ye, Y., 2015. Application of seismic complex decomposition on hydrocarbon detection, in *Proceedings of the 77th EAGE Conference and Exhibition*, EAGE Expanded Abstract, Tu P6 02, Madrid, Spain.

Lüth, S., Ivanova, A. & Kempka, T., 2015. Conformity assessment of monitoring and simulation of CO_2 storage: a case study from the Ketzin pilot site, *Int. J. Greenhouse Gas Contl.*, **42**, 329–339.

Martens, S., Möller, F., Streibel, M., Liebscher, A. & the Ketzin Group, 2014. Completion of five years of safe CO_2 injection and transition to the post-closure phase at the Ketzin pilot site, *Energy Procedia*, **59**, 190–197.

Norden, B. & Frykman, P., 2013. Geological modelling of the Triassic Stuttgart Formation at the Ketzin CO_2 storage site, Germany, *Int. J. Greenhouse Gas Contl.*, **19**(0), 756–774.

Norden, B., Förster, A., Vu-Hoang, D., Marcelis, F., Springer, N. & Le Nir, I., 2010. Lithological and petrophysical core-log interpretation in CO_2SINK, the European CO_2 onshore research storage and verification project, *SPE Reservoir Eval. Engineer.*, **13**(02), 179–192.

Partyka, G., Gridley, J. & Lopez, J., 1999. Interpretational applications of spectral decomposition in reservoir characterization, *Leading Edge*, **18**(3), 353–360.

Ravazzoli, C.L. & Gómez, J.L., 2014. Seismic reflectivity in carbon dioxide accumulations: a review, in *CO_2 Sequestration and Valorization*, chap. 12, pp. 343–360, ed. Esteves, V., InTech, doi:10.5772/57087.

Sturton, S., Buddensiek, M. & Dillen, M., 2010. AVO analysis of thin layers—application to CO_2 storage at Sleipner, in *Proceedings of the 72nd EAGE Conference and Exhibition incorporating SPE EUROPEC*, Barcelona, Spain.

Swan, H.W., 1991. Amplitude-versus-offset measurement errors in a finely layered medium, *Geophysics*, **56**(1), 41–49.

White, J.C., Williams, G.A. & Chadwick, R.A., 2013. Thin layer detectability in a growing CO_2 plume: testing the limits of time-lapse seismic resolution, *Energy Procedia*, **37**, 4356–4365.

White, J.C., Williams, G.A., Grude, S. & Chadwick, R.A., 2015. Utilizing spectral decomposition to determine the distribution of injected CO_2 at the Snøhvit Field, *Geophys. Prospect.*, **5**(63), 1213–1223.

Williams, G. & Chadwick, A., 2012. Quantitative seismic analysis of a thin layer of CO_2 in the Sleipner injection plume, *Geophysics*, **77**(6), R245–R256.

APPENDIX: THEORY OF COMPLEX SPECTRAL DECOMPOSITION

In accordance with the convolution model, a seismic trace **s** in the time domain can be represented by a source wavelet convolved with a reflectivity series. Considering the case of multiple wavelets (Bonar *et al.* 2010), the seismic trace can be constructed by the summation of convolutions of N distinct wavelets **w** with the corresponding reflectivity sequences **r** and the addition of random noise **n**. In order to include phase information, a complex wavelet library can be built by transforming the real-valued wavelets with the Hilbert transform. Consequently, the seismic trace is given by

$$\mathbf{s} = \sum_{i=1}^{N} [\mathbf{w}_i * \mathbf{r}_i] + \mathbf{n}, \tag{A1}$$

where $*$ represents convolution, $\mathbf{w}_i$ is the ith complex wavelet with dominant frequency f and phase φ_w, $\mathbf{r}_i$ is the corresponding complex reflectivity series with the components of frequency f and phase φ_r. According to the phase property of deconvolution, the phase

Downloaded from http://gji.oxfordjournals.org/ at Bibliothek des Wissenschaftsparks Albert Einstein on September 19, 2016

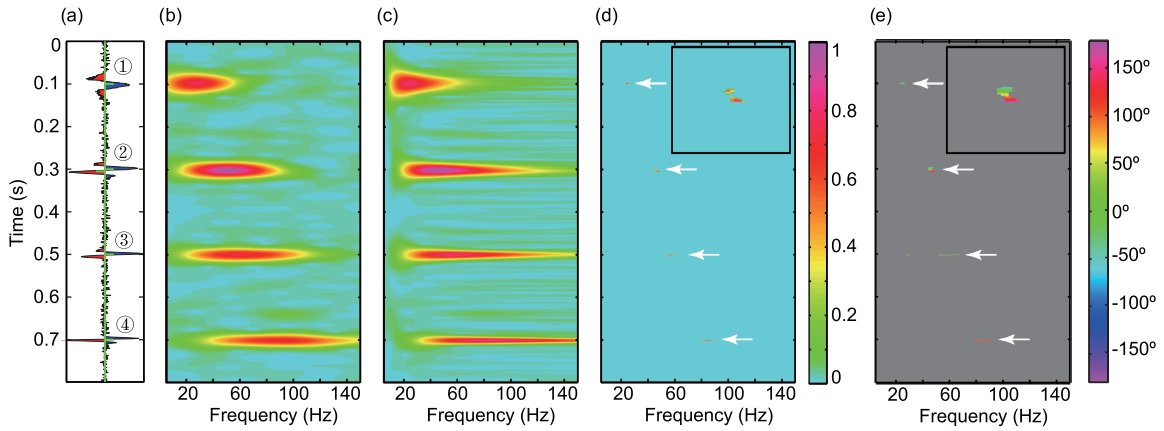

Figure A1. Spectral decomposition of a synthetic trace contaminated with random noise (signal-to-noise ratio: 3.6). (a) Synthetic seismogram with the generated reflectivity series (green line). Time–frequency spectra decomposed by (b) the Gabor transform, (c) CWT and (d) complex spectral decomposition. (e) Wavelet phase spectrum decomposed by complex spectral decomposition. Inset shows the zoom of the second reflection.

component of the seismic trace will be maintained in the complex reflectivity series if the complex wavelet library is constructed by zero-phase wavelets ($\varphi_w = 0$).

In matrix form, the above equation can be written as

$$\mathbf{s} = (\mathbf{W}_1\ \mathbf{W}_2 \cdots \mathbf{W}_N) \begin{pmatrix} \mathbf{r}_1 \\ \mathbf{r}_2 \\ \vdots \\ \mathbf{r}_N \end{pmatrix} + \mathbf{n}, \tag{A2}$$

where $\mathbf{W}_i$ is the convolution matrix of the complex wavelet $\mathbf{w}_i$.

Eq. (A2) can also be expressed as a product of the convolution matrix of the complex wavelet library $\mathbf{W}$ and reflectivity sequences as

$$\mathbf{s} = \mathbf{W}\mathbf{r} + \mathbf{n}. \tag{A3}$$

Determination of the reflectivity sequences $\mathbf{r}$, namely the complex time–frequency spectrum including phase and dominant frequency information, from eq. (A3) is an underdetermined inverse problem. The L1 norm has a sparsity-inducing property, and therefore L1-norm regularization is applied to the cost function J (eq. A4) in order to obtain the time–frequency spectrum concentrated around the centre of the wavelets (Bonar & Sacchi 2010)

$$J = \frac{1}{2}\|\mathbf{W}\mathbf{r} - \mathbf{s}\|^2 + \lambda\|\mathbf{r}\|_1, \quad \lambda > 0, \tag{A4}$$

where the least square term is the prediction error and λ is the regularization parameter which manipulates the L1 norm to affect the solution sparsity. In order to reduce the required computational time, a fast iterative soft-thresholding algorithm (Beck & Teboulle 2009) is used to solve the cost function.

Fig. A1 shows a comparison of the complex spectral decomposition spectrum with the Gabor transform and CWT spectra. The first reflection in the synthetic trace is generated by convolving a 25 Hz dominant frequency Ricker wavelet phase shifted by -30° with a positive reflection coefficient located at 0.1 s. The second reflection results from a zero-phase Ricker wavelet of 40 Hz dominant frequency convolved with a reflectivity pair. For the reflectivity pair, the positive reflection coefficient is placed at 0.3 s with a reflection coefficient of opposite polarity and of equal magnitude 5 ms later. The third and fourth reflections are generated by the convolution of a 60 Hz 50° phase shifted Ricker wavelet and an 85 Hz 125° phase shifted Ricker wavelet with positive reflectivity sequences placed at 0.5 and 0.7 s, respectively. Gaussian noise is introduced to the synthetic trace in order to test the noise sensitivity. In comparison with the Gabor transform and CWT methods, the complex spectral decomposition result has significantly higher time–frequency resolution and is less affected by random noise. The reflective energy concentrates around the corresponding dominant frequencies and resolves the reflectivity pair of the second reflection. In addition, the phase spectrum obtained by complex spectral decomposition correctly reveals the phase information of the synthetic signals.

Downloaded from http://gji.oxfordjournals.org/ at Bibliothek des Wissenschaftsparks Albert Einstein on September 19, 2016